Materials Research. 2023; 26: e20220529
DOI: https://doi.org/10.1590/1980-5373-MR-2022-0529

Numerical Prediction for the Effects of Welding Interpass Temperature on the Thermal History and Microstructure of Duplex Stainless Steels

Carlos Roberto Xavier[a]*, Horácio Guimarães Delgado Junior[b], Matheus Gomes Rebello[a],

Raí Ramos Lisbôa[a], Ana Carolina Martins Silva[c], José Adilson de Castro[c]

[a]Centro Universitário de Volta Redonda (UniFOA), Departamento de Engenharia Mecânica, Av. Paulo E. A. Abrantes, 1325, Três Poços, 27240-560, Volta Redonda, RJ, Brasil.
[b]Universidade do Estado do Rio de Janeiro (UERJ), Faculdade de Tecnologia, Departamento de Mecânica e Energia, Rod. Pres. Dutra, Km 298, 27537-000, Resende, RJ, Brasil.
[c]Universidade Federal Fluminense (UFF), Programa de Pós-Graduação em Engenharia Metalúrgica (PPGEM), Av. dos Trabalhadores, 420, Vila Santa Cecília, 27255-125, Volta Redonda, RJ, Brasil.

Received: December 08, 2022; Revised: March 26, 2023; Accepted April 21, 2023

Numerical simulation was used to predict the thermal behavior and the resulting microstructure at the heat-affected zone (HAZ) of a 170 mm diameter and 3.5 mm thickness super duplex stainless steel (SDSS) UNS S32750 tube. In order to evaluate the thermal response from the model, a usual welding situation involving interpass temperature (IT) and its influence on the HAZ microstructure was exploited. Thus, two superimposed autogenous welding passes were simulated, the first clockwise with the tube in the room temperature and the second, counterclockwise, with the tube at the temperature of 250ºC. Even subjected to successive thermal cycles and high interpass temperature, the proportion and morphology of the phases at the HAZ and Fusion Zone (FZ) did not present significant differences when comparing the two welding passes. Meanwhile, nitrogen losses should be avoided during welding in order to obtain a balanced microstructure in DSS welds, contributing to guarantee satisfactory toughness in addition to resistance to pitting corrosion. The predictions from the simulation were validated by using experimental results obtained from the autogenous TIG (Tungsten Inert Gas) process.

Keywords: *Welding interpass temperature, duplex stainless steel, numerical simulation, thermal history, microstructure.*

1. Introduction

Duplex stainless steels (DSS) present an excellent combination of strength and toughness together with high resistance to pitting corrosion and stress corrosion. These properties combined with a competitive cost enable DSS to be an outstanding material for applications where high performance is required, such as in the chemical, petrochemical, petroleum, food, and power generation industries[1]. On the other hand, it is well known that the DSS properties depend on the austenite-ferrite ratio, which is designed to be approximately 1:1, while their mechanical properties are commonly determined by the single-phase properties of ferrite and austenite and by the spatial distribution of constituents in the two-phase alloy[2]. However, despite the austenite-ferrite ratio previously mentioned, the DSS application is still acceptable when any of the mentioned phases are not present with less than 30% in their microstructure[3]. Despite the excellent properties of DSS, they can be subjected to a welding procedure at any time aiming toward the manufacture or repair of equipment, systems or structures, which can lead to localized microstructural changes, impairing their acclaimed properties. In addition to the change in the balance between the ferrite and austenite phases, deleterious precipitates, such as sigma (σ) and chi (χ) phases can occur as a result of the thermal history and thermal cycles to which the weldment has been subjected, resulting in detrimental effects on corrosion resistance and impact toughness of DSS. In this regard, notwithstanding the fact that the sigma phase is detrimental to the corrosion resistance and impact toughness of DSS[4], it is worth noting that even small amounts of sigma phase, such as 1%, would be sufficient to cause a drastic reduction in the impact toughness of these steels[5,6]. Thus, one of the ways to obtain a welded joint with acceptable properties is by controlling the thermal history developed during welding, which in the case of DSS is done by limiting the welding interpass temperature to 100º C[3]. However, this interpass temperature limitation prevents the search for increased productivity during the DSS welding, once the execution of a newly welding pass is very time consuming since it is required to be below 100 °C, which led to Alvarez et al.[7] to evaluate the influence the use of interpass temperature between 150 and 290 °C on the properties of DSS during welding, using a UNS S31803 DSS for this purpose. The authors[7] found the values of impact toughness were lower as the notch approached the center of the weld and attributed this result to the influence of the successive thermal cycles and high interpass temperature, while the values of CPT (Critical

*e-mail: carlos.xavier@foa.org.br

Pitting Temperature) in the root were much lower than in the BM (Base Metal), which could also be attributed to the same causes previously mentioned. Lee et al.[8] observed that increasing welding interpass temperature (until 250°C) favored the pitting formation and associated this result with the second phases formation and reported that the pit was preferentially formed in austenite, since it presented a lower PREN (Pitting Resistance Equivalent Number) in comparison com ferrite. As it is known, the PREN has a dependence on the nitrogen content according to the relationship: PREN = Cr (wt%) + Mo (wt%) + 16 N (Cr%), which leads anyone to conclude that a possible loss of nitrogen could have occurred when successive high thermal cycles and elevated welding interpass temperature were imposed to the weld metal. In fact, Alvarez et al.[7] reported that the nitrogen content measured was 31% lower in weld root comparatively to the base metal, which led them to conclude the loss of this alloying as a consequence of successive reheating. Thus, one of the ways to compensate eventual losses of nitrogen during welding would be, for example, to ensure the presence of this alloying in the composition of the shielding gases, as discussed by Xavier et al.[1] which, in addition of promoting an adequate balance in the weld microstructure, could also avoid lower PREN values.

Accordingly, the modeling and simulation of the welding have proved to be an essential tool for a better understanding of how thermal, mechanical, and metallurgical phenomena act separately and together, influencing the weldment properties[9-11]. Furthermore, modeling and simulation of the welding also can provide cost and time reduction, since it can avoid the sometimes long and expensive laboratory experiments and tests, in addition to the possibility of improving the quality of the final product[12]. Following this matter, Hemmer and Grong[13] modeled the microstructural evolution in DSS under thermal conditions applicable to welding, such as the austenite dissolution during heating, grain growth in delta ferrite and the decomposition of delta ferrite to austenite during cooling. Ferro and Bonollo[14], proposed a semiempirical model for sigma phase precipitation in duplex and superduplex stainless steel under isothermal and nonisothermal conditions. Their model gives a satisfactory estimation of sigma phase precipitates during both isothermal aging and the continuous cooling process. Hertzman et al.[15] applied a theoretical model based on the paraequilibrium concept and in the Cahn theory for grain boundary nucleated reactions and have obtained essential information on the weld metal composition influence, outstandingly the nitrogen, on the austenite reformation occurring at the HAZ of DSS during welding. Xavier et al.[1] evaluated essential microstructural changes occurring in DSS during welding, which were supported by numerical simulation. For this purpose, the numerical model took into account the prediction of the temperature field dynamically coupled with the welding process evolution and the material thermophysical properties.

2. Materials and Methods

2.1. Materials

In this study, a UNS S32750 SDSS tube with 170 mm external diameter and 3.5 mm thickness was used. The chemical composition of the SDSS is shown in Table 1.

2.2. Experimental

A mechanized autogenous TIG welding process was carried out using an inverter device for TIG AC/DC welding model CastoTig 2003 AC/DC. The welding parameters and corresponding heat input are presented in Table 2 with argon being used as the shielding gas. The UNS S32750 SDSS tube received two overlapping welding passes, using the chosen interpass temperature, i.e., 250°C, which is the variable of interest for this study (Figure 1).

The first welding pass (clockwise) was carried out at room temperature around the complete tube circumference. The second welding pass (counterclockwise), using the previously defined interpass temperature, returned from the end of the first welding pass. In both welding passes the thermal cycles were measured by using thermocouples inserted into the UNS S32750 SDSS tube and recorded it by a PC based high speed data acquisition unit. The second welding pass aimed to evaluate the influence of reheating on the HAZ transformations. Thus, a minor heat input was used to avoid damage or until the destruction of HAZ previously formed during the first welding pass. The aim was also to reproduce the results occurring during the usual field welding procedure with satisfactory accuracy.

Samples for metallographic analysis were taken perpendicular to the weld bead and identified according to the position of the thermocouples in the tube (Figure 1). After that, sample surfaces were sanded with silicon carbide sandpaper and polished respectively with 6, 3, and 1 μm grade diamond paste. The sample's microstructure was revealed through chemical etching using Beraha's modified solution, which consists of 80 ml of distilled water (H_2O), 20 ml of

Table 1. UNS S32750 SDSS tube chemical composition (wt. %).

C	Mn	Si	P	S	Cr	Ni	Mo	Cu	N
0.023	0.77	0.46	0.023	0.007	25.32	7.43	3.94	0.49	0.24

Table 2. Welding parameters.

Welding pass	Arc voltage (V)	Welding current (amp)	Welding speed (mm s^{-1})	Thermal efficiency (η)	Heat input (kJ mm^{-1})
Clockwise*	13.1	178.1	4.1	0.8	0.45
Counterclockwise**	14.2	179.8	8.2	0.8	0.25

*Room Temperature; **Welding interpass temperature: 250°C

hydrochloric acid (HCl), 2 g of potassium metabisulfite ($K_2S_2O_5$) and 2 g of ammonium bifluoride (NH_4HF_2), for a time of 10 seconds.

Microstructural analysis from the BM, HAZ and FZ was carried out through scanning electron microscopy (SEM) and optical microscopy (OM) using, respectively, a ZEISS EVO MA10 scanning electron microscope and an Olympus optical microscope, while micrographics images following the ASTM E-562-19[16] standard served to calculate the respective volume fractions of the austenite and ferrite phases using 16-point grids on each image.

2.3 . Modeling principles, initial and boundary conditions

The mathematical model is constructed to dynamically predict the temperature, thermophysical properties, and phase transformations in a three-dimensional domain representing the steel pipe and the weld bead deposition. The geometrical changes due to the bead formation are considered dynamically together with the local changes of the thermophysical properties assumed, depending on the temperature, phase formations, and local steel composition. The mass transfer in the welding pool is due to metal deposition and melting with subsequent re-solidification which are locally considered during the transient calculation. The energy is transferred from the torch to the metal piece while the cooling effects are due to the endothermic transformations and thermal exchange with the environment, promoting the thermal cycle leading to phase transformations.

Equation 1 represents the energy balance in the working peace using a generalized coordinate system and whose numerical implementation details for its solution can be found in other works by the authors[1,12,17,18].

$$\frac{\partial}{\partial t}\left(\rho C_p T\right)+\frac{\partial}{\partial x_i}\left(u_i \rho C_p T\right)=\frac{\partial}{\partial x_i}\left(\frac{k}{C_p}\frac{\partial T}{\partial x_j}\right)+Q_v+Q_T \quad (1)$$

where the indexes i and j represent the directions of the coordinate axis, ρ is the material density; C_p is the temperature-dependent material-specific heat capacity; k is the local temperature-dependent thermal conductivity of the material and $\boldsymbol{u}$ is the velocity components, which dynamically takes into account the buoyancy-driven motion in the liquid pool or due to the motion of the mesh to fit the bead formation and geometry changes due to the addition of metal. T is the local temperature. The volumetric energy source due to the torch is spatially represented by $Q_v = q_r + q_f$, and the energy involved during the phase transformations is termed Q_T.

The volumetric energy input due to the torch is mathematically modeled by the energy volumetric spatial variation given by adapting the Goldak moving double ellipsoid function in a three-dimensional frame (Figure 2)[19].

The volumetric heat input is a combination of two moving ellipsoids referenced in a local moving coordinate system: one in the rear quadrant and another in the superposition of the front quadrant of the moving heat source, as presented by Equations 2 and 3, respectively. The thermal energy due to the arc is distributed by a function of time and position by selecting a few parameters based on the experimental works.

$$q_f(x,y,z)=\frac{6\sqrt{3}f_f Q}{ab_f c\pi\sqrt{\pi}}e^{-3\left(\frac{x}{a}\right)^2}e^{-3\left(\frac{y}{b_f}\right)^2}e^{-3\left(\frac{z}{c}\right)^2} \quad (2)$$

$$q_r(x,y,z)=\frac{6\sqrt{3}f_r Q}{ab_r c\pi\sqrt{\pi}}e^{-3\left(\frac{x}{a}\right)^2}e^{-3\left(\frac{y}{b_r}\right)^2}e^{-3\left(\frac{z}{c}\right)^2} \quad (3)$$

The total amount of energy furnished to the working peace $Q = \eta VI$ is specified by measured operational variables of current (I), voltage (V), and estimated process efficiency (η) respectively (see Table 2). The source energy factors f_f,

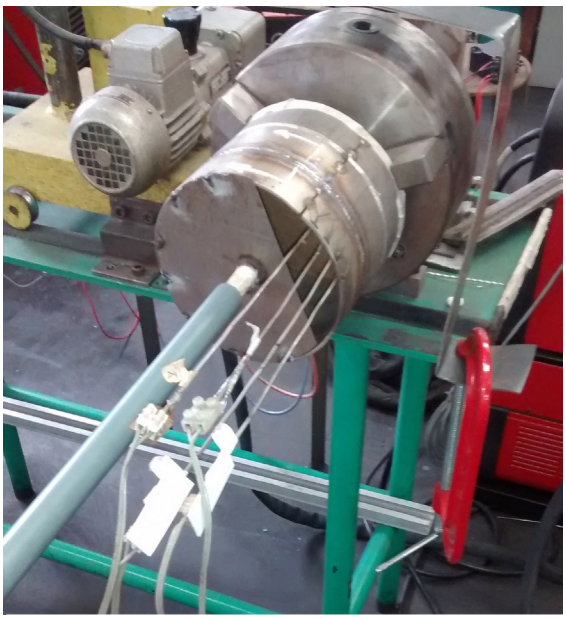

Figure 1. Experimental welding of UNS S32750 SDSS tube (two overlapping autogenous welding pass were carried out: clockwise and counterclockwise).

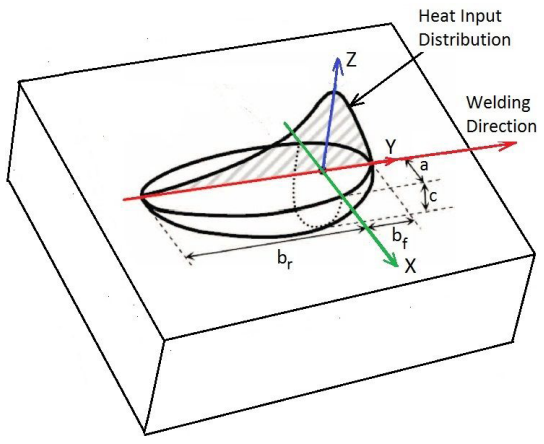

Figure 2. The dynamic spatial distribution of the double-ellipsoid energy volumetric source[19].

f_r represent the portions of the heat furnished in the front and rear quadrants respectively, which are selected to attain the restriction of $f_r + f_r = 2$, while the *a*, *b* e *c* are geometric heat constants that define the size and shape of the ellipsoids, hence the spatial and temporal heat source distributions are localized during the torch motion characterizing the dynamics of the welding procedure.

The boundary conditions for cooling between the workpiece and the environment through convection and radiation are calculated by Equations 4 and 5, respectively.

$$q_{\text{convection}} = h_{\text{eff}}\left(T - T_{\text{environment}}\right) \quad (4)$$

$$q_{\text{radiation}} = \varepsilon\sigma\left(T^4 - T^4_{\text{environment}}\right) \quad (5)$$

The environment temperature was assumed to be 25°C, the material emissivity ε (0.6) and σ =5.67x10^{-8} *W. m^{-2}.K^{-4}* is the constant of Stefan-Boltzmann. In this study, the effective heat transfer coefficient h_{eff} was assumed to be 15 *W. m^{-2} K^{-4}*.

The dynamic changes in the material properties were assumed to be temperature-dependent. The used averaged local variations of the heat capacity (C_p) and thermal conductivity of the steel (k) are shown in Figures 3a and 3b assumed in this study for the UNS S32750 SDSS. The density of the UNS S32750 SDSS was assumed to be 7800 *kg.m^{-3}*.

The authors have developed their own computational program which has been updated for different applications and new features are introduced, as demanded, depending on the welding procedure or materials used. In this paper, the new implementations which were carried out, are related to the materials properties calculations, the geometry of the workpiece (pipe), and the corresponding coordinates of the local moving heat source distribution.

The solutions of Equations 1 to 5 are iteratively obtained using the finite volume technique. The implementation was made in a self-developed computational source code which has been continuously updated for over 15 years by the authors. The implementations and model validations have been performed for different materials under a variety of boundary conditions representing particular weldment procedures, geometries, and materials[1,12,17,18].

3. Results and Discussion

3.1 . Thermal aspects

Temperature distribution on the UNS S32750 SDSS tube using the welding interpass temperature evaluated in this study can be seen in Figures 4a and 4b. Two superimposed weld passes were simulated, the first being clockwise (Figure 4a) and the second, counterclockwise (Figure 4b)

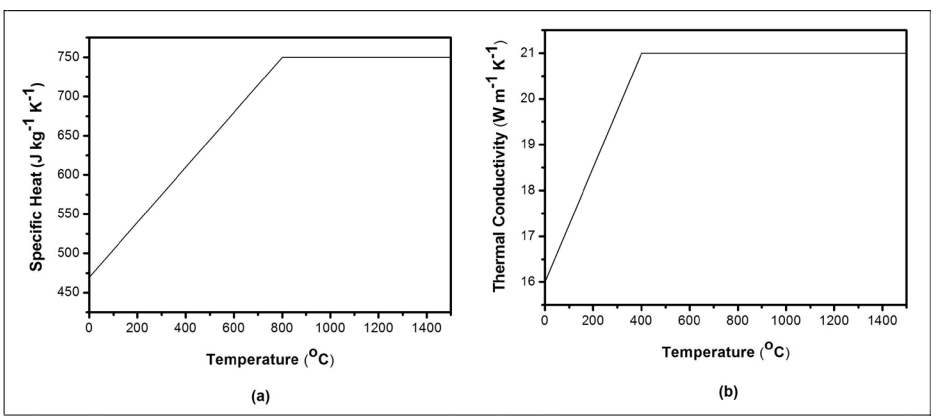

Figure 3. Assumed SDSS UNS S32750 thermophysical properties: (a) specific heat and (b) thermal conductivity.

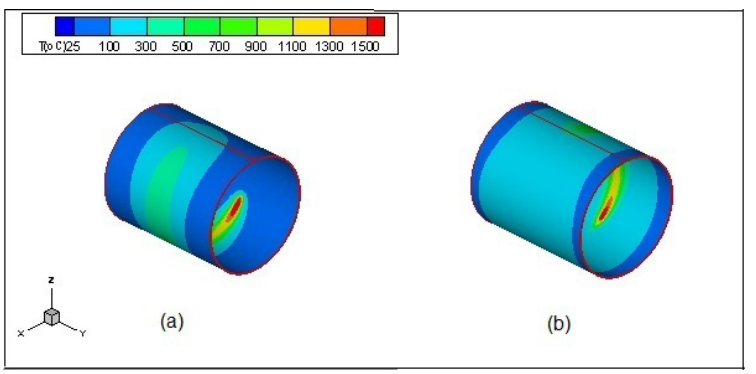

Figure 4. Temperature distribution in UNS S32750 SDSS tube: (a) clockwise and (b) counterclockwise welding pass.

with the latter in a condition where the tube temperature was set at 250°C, corresponding to the chosen welding interpass temperature. It can be observed that during the clockwise welding pass, the heat is more concentrated around the welding source, i.e., the isothermals are narrower, leading to larger temperature gradients and affecting the cooling rates. In turn, during the counterclockwise welding pass, the heat is more dissipated in relation to the welding source i.e., the isothermals are wider leading to lower temperature gradients and also affecting the cooling rates. Thus, the discussion is valid in order to demonstrate the welding effects without (clockwise welding pass) and with welding interpass temperature (counterclockwise welding pass) on the tube cooling rates and, consequently, on the resulting microstructure at the HAZ.

Meanwhile, in Figure 5, the calculated and measured welding thermal cycles at an arbitrary location of the HAZ can be compared in both cases, i.e., at room temperature (clockwise) and with welding interpass temperature (counterclockwise). As previously discussed, the cooling rates are higher in the clockwise welding pass, the condition where the procedure was performed at room temperature, therefore, justifying higher thermal gradients. Thus, the welding interpass temperature has the characteristic of affecting the workpiece cooling rate, which can be exploited to control the HAZ microstructure and, accordingly, its properties. In Figure 5, the reason for the temperature peak corresponding to the counterclockwise welding pass to remain below of peak associated with the clockwise welding pass is that a minor heat input was intentionally used (Table 2), since it aimed only at the reheating of the preexisting HAZ (formed in clockwise welding pass).

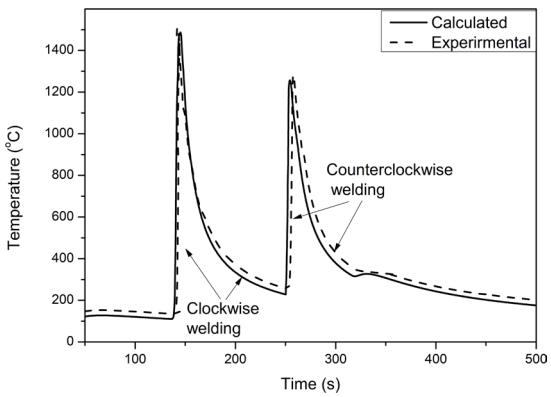

Figure 5. Comparing the thermal cycles (calculated and measured) at the HAZ during clockwise and counterclockwise welding passes.

3.2 . Microstructure

3.2.1. Base metal

Figure 6 shows the microstructure corresponding to the UNS S32750 SDSS tube using OM (Figure 6a) and SEM (Figure 6b). The base metal microstructure consists of alternating lamellar grains of austenite in a ferritic matrix, whose proportion between the ferrite and austenite phases was 48.3%±1.2% and 51.7%±1.3% respectively and no evidence of the sigma phase presence was noticed at the BM microstructure using OM and SEM.

3.2.2. Heat-affected zone

Figure 7a and 7b corresponds to the sequence of welding in the clockwise direction with the respective comparisons of the dimensions of the HAZ and FZ obtained by means of numerical simulation and experimentally (Figure 7e), besides the corresponding associated thermal cycles (Figure 7g). On the other hand, Figure 7c and 7d corresponds to the sequence of welding in the counterclockwise direction and use of interpass temperature, with the respective comparisons of the dimensions of the HAZ and FZ obtained by means of numerical simulation and experimentally (Figure 7f), besides of corresponding associated thermal cycles (Figure 7g). It is important to highlight that due to the use de minor heat input in the counterclockwise welding that the HAZ and FZ dimensions are smaller in this step, as it can be seen in Figures 7e and 7f. The reason for use of minor heat input in the counterclockwise welding is that it aimed only to promote the reheating of the HAZ previously formed (clockwise welding) in order to evaluate the effects of successive thermal cycles and elevated interpass temperature in the transformations that occur in this weld region. In both conditions (clockwise and counterclockwise welding) the HAZ microstructure was composed by austenite with different morphologies,

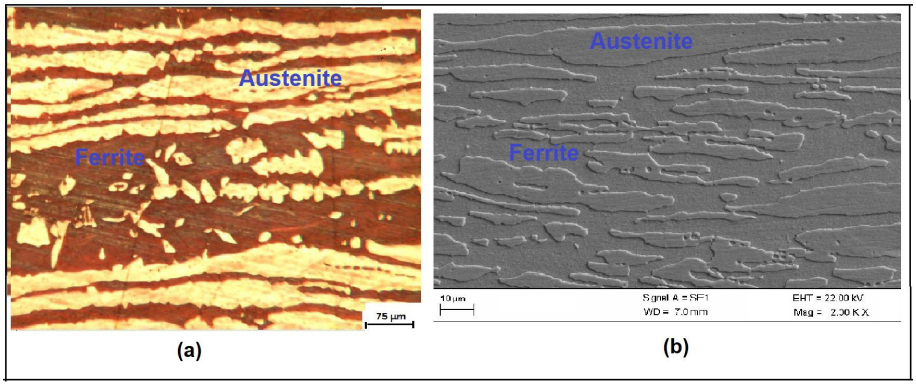

Figure 6. UNS S32750 SDSS microstructure using a) OM: austenite and ferrite (dark phase) and (b) SEM.

including allotriomorphic (AA) or grain boundary (GBA) austenite; Widmanstätten austenite (WA), which can nucleate from allotriomorphic austenite and grows along the ferritic matrix and intragranular austenite (IA) precipitated at the ferrite as it can be seen in Figures 7h and 7i respectively.

Furthermore, as can also be seen in Figures 7h and 7i, there was no meaningful variation in the austenite content when comparing the clockwise and counterclockwise welding passes, in addition to the no observance of the sigma phase presence in the HAZ microstructure using OM (Figure 7) and SEM (Figure 8).

In fact, the ferrite volume fraction in the clockwise welding pass was 51.8% ± 1.1%, while in the counterclockwise welding pass (using interpass temperature of 250°C), it was 50.3% ± 1.2%. These results also demonstrate that there was no significant difference in relation to that found for the BM, justifying little influence of welding interpass temperature on the proportions of the phases in HAZ, as it was also related by Alvarez et al.[7]. The observations related to the austenite volume fraction in the HAZ and the non-observance of the sigma phase in this same region can be justified through Figures 9 and 10 respectively, which had the effective influence of the thermal behavior from the UNS S32750 SDSS tube during welding as discussed in the previous section. For this purpose, a diagram during continuous cooling transformation (CCT) of a similar SDSS 24.5 Cr/7 Ni and 0.20% N[20] was used. Figure 9 shows the cooling curves calculated and plotted from a temperature at the HAZ where the ferrite-austenite transformation takes place and it has presented very similar rates despite having been used a welding interpass temperature of 250°C in the counterclockwise pass which, however, has provided a slightly lower cooling rate. This finding favors the ferrite-austenite transformation, which would explain the minor ferrite content in the counterclockwise welding pass as previously mentioned.

Meanwhile, Figure 10 corresponds to the use of the diagram for the formation of 1% of the sigma phase during continuous cooling transformation (CCT) for an equivalent SDSS SAF 2507[21] with the cooling curves calculated in this study and plotted from a temperature in HAZ where sigma phase precipitation can occur in UNS S32750 SDSS, both in the clockwise and counterclockwise welding passes, with the latter using a welding interpass temperature of 250°C. As can be seen in Figure 10, the cooling rates were below that necessary for the formation of at least 1% of the sigma

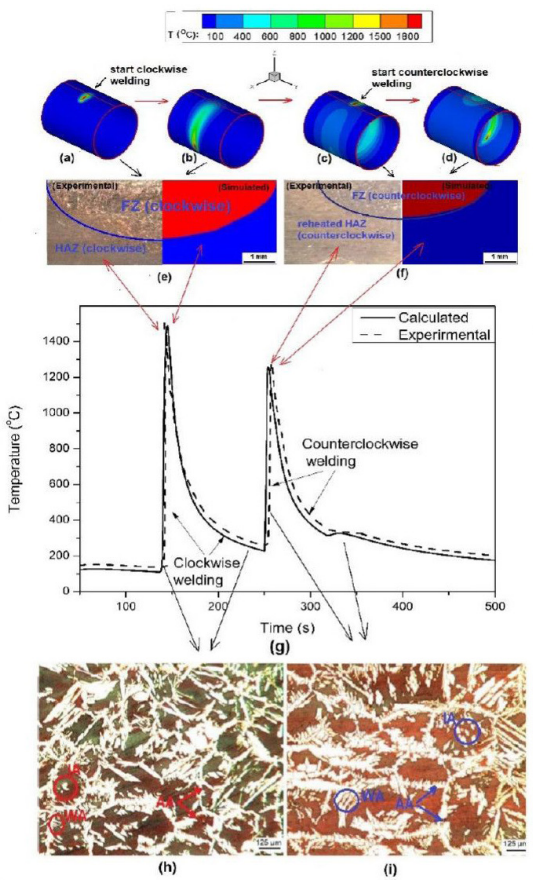

Figure 7. Correlation among: a-d) welding procedure; e-f) resulting dimensions for HAZ and FZ (comparing experimental and simulated); g) resulting thermal cycles (comparing experimental and simulated) and h-i) resulting microstructure in HAZ (experimental).

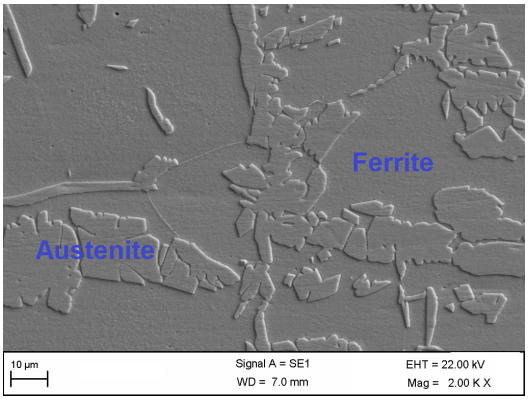

Figure 8. HAZ microstructure by SEM in the counterclockwise welding pass (IT: 250°C): ferrite and austenite.

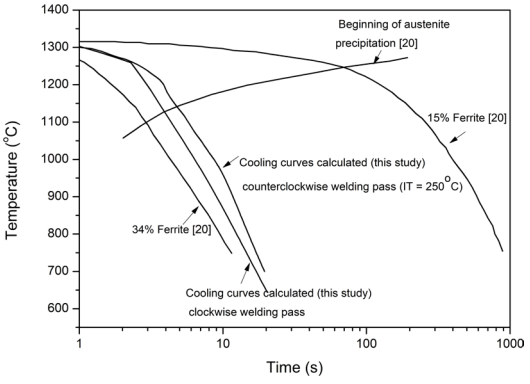

Figure 9. Ferrite content prediction in HAZ using a similar CCT diagram for SDSS 24.5% Cr/7% Ni and 0.20% N[20].

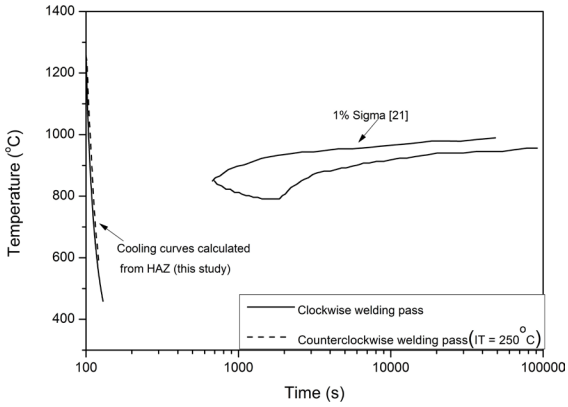

Figure 10. Sigma phase prediction in HAZ using a CCT diagram for an equivalent SDSS SAF 2507[21].

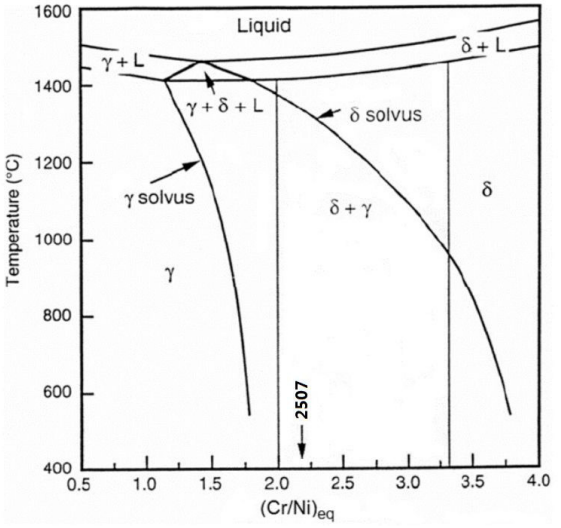

Figure 11. Pseudo-binary diagram based on WRC-1992 equivalent relationships[22]

phase in both the clockwise and counterclockwise welding passes, even using the interpass temperature of 250°C in this latter, justifying the non-observance of the referred metallic compound by using metallographic analysis (Figures 7 and 8).

In fact, both results presented by the Figures 9 and 10 may be corroborated by using the Figure 7(g), since little difference was observed in relation to the respectively cooling curves when applying, or not, the welding interpass temperature, independently of the peak temperature reached in each one of the mentioned situations.

3.2.3. Fusion zone

Phenomena as rapid heating and metal localized fusion caused by the energy supplied by the welding source allied to locally elevated cooling rates may seriously affected the final microstructure of FZ, impairing the balanced fraction between the austenite and ferrite phases present in the parent metal, which can degrade the attractive properties of the DSS.

In Figure 11, it can be seen that the ferrite is the only phase forming directly from the liquid for an equivalent 2507 SDSS[22], with the subsequent transformation ferrite-austenite occurring when the alloy achieves de solvus line. Figure 12 corresponds to the microstructure from the FZ during clockwise (Figure 12a) and counterclockwise (Figure 12b) welding pass. In both situations the microstructure is formed by large columnar ferrite grains at the presence of several morphological types of austenite, as allotriomorphic austenite (AA), Widmanstätten austenite (WA) and intragranular austenite (IA), while the fractions of ferrite were 48% ± 1.3% in the clockwise and 52% ± 1.2% in the counterclockwise welding pass respectively and no evidence of sigma phase was noticed at the FZ by OM (Figure 12) and SEM (Figure 13). Although the difference observed in the ferrite fractions between the welding passes (clockwise and counterclockwise) is small, a possible explanation for the lower content of austenite at the FZ in the counterclockwise welding pass is in the loss of alloying during successive welding passes, such as nitrogen, since this element is a strong austenite former[23-25], having even been reported by Alvarez et al.[7] that nitrogen content measured in weld root was 31% lower relatively to the base

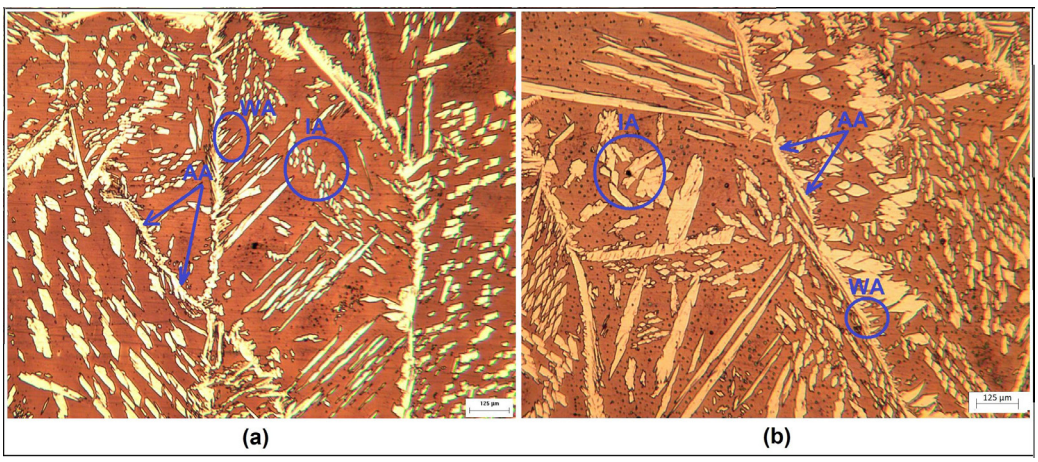

Figure 12. FZ microstructure by OM (a) clockwise and (b) counterclockwise welding pass (IT: 250°C).

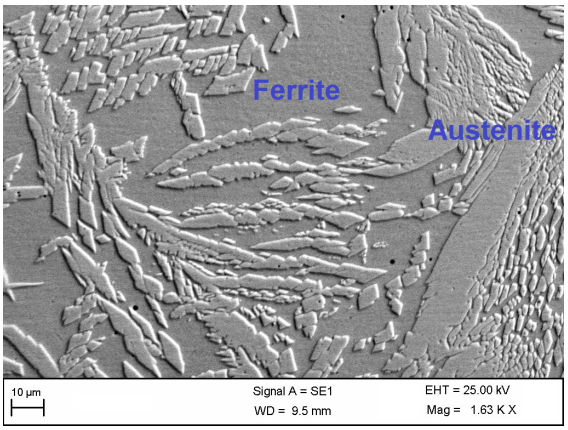

Figure 13. FZ microstructure by SEM in the counterclockwise welding pass (IT: 250°C): ferrite and austenite.

metal and attributed this finding as consequence of successive reheating experimented by that weld region. It is worth mentioning that there seems to be a competition between the effects of nitrogen and cooling rates on the austenite formation at the FZ of UNS S32750 DSS, since the results are in opposing to the expected effects of slower cooling rates caused by the adoption of welding interpass temperature, which would favor the austenite reform and, therefore, a greater volume fraction of this phase when compared to the clockwise welding pass. In fact, Xavier et al.[1] evaluated the associated effects of nitrogen to different cooling rates on the formation of austenite at the FZ in DSS and concluded by the strong influence of this element, not only on the austenite volume fraction but also on the morphology of this phase.

4. Conclusion

A study to evaluate the resultant microstructure at the HAZ and FZ of a SDSS was carried out based on experimental and numerical simulation. By using the numerical simulation, it was possible to predict the thermal history and to locally calculate the heating and cooling rates occurring when a UNS S32750 SDSS tube was submitted to a procedure involving welding interpass temperature of 250°C. Thus, the main findings are summarized as follows.

a) The model was able to quite accurately predict the thermal behavior during welding.
b) The combined method of using the results obtained through numerical simulation, together with transformation diagrams during continuous cooling, showed to be able to satisfactorily predict the resulting microstructure at the HAZ, which was confirmed through experimental results.
c) No evidence of sigma phase precipitation has occurred and an adequate balance between ferrite and austenite phases was maintained at the HAZ microstructure.
d) The nitrogen plays a key role in the transformations occurring in the FZ during the welding of DSS and must be maintained at identical levels to the BM in order to guarantee a balanced microstructure and, accordingly, to ensure its attractive properties as toughness and corrosion resistance.
e) Despite not having been evidenced the presence of the sigma phase at the HAZ and FZ, it is still very important to evaluate the presence of others deleterious precipitates, such as the Cr_2N in welds of DSS, since some works reported a significant reduction in their key properties as the toughness and pitting resistance.

5. Acknowledgments

This work was partially supported by CNPq, FAPERJ and CAPES.

6. References

1. Xavier CR, Delgado HG Jr, Castro JA. An experimental and numerical approach for the welding effects on the duplex stainless steel microstructure. Mater Res. 2015;18(3):489-502.
2. Morales EV, Betancourt G, Olaya L, Bott IS. Some insight on the heat-affected zone strengthening mechanisms in duplex stainless Steels. Mater Res. 2022;25:e20210553.
3. Standards Norway. NORSOK Standard M-601: welding and inspection of piping. Norway: Standards Norway; 2016.
4. Tan H, Jiang Y, Deng B, Sun T, Xu J, Li J. Effect of annealing temperature on the pitting corrosion resistance of super duplex stainless steel UNS S32750. Mater Charact. 2009;60:1049-54.
5. Chen TH, Weng KL, Yang JR. The effect of high-temperature exposure on the microstructural stability and toughness property in a 2205 duplex stainless steel. Mater Sci Eng A. 2002;338(1-2):259-70.
6. Sieurin H, Sandström R. Sigma phase precipitation in duplex stainless steel 2205. Mater Sci Eng A. 2007;444:271-6.
7. Alvarez TR, Pavarino MRC, Souza GC, Pardal JM, Tavares SSM, Ferreira MLR, et al. Influence of interpass temperature on the properties of duplex stainlesssteel during welding by submerged arc welding process. Welding International. 2016;30(5):348-58.
8. Lee B-H, Lee H-W, Shin Y-T. Intergranular corrosion characteristics of super duplex stainless steel at various interpass temperatures. Int J Electrochem Sci. 2015;(10):7535-47.
9. Khalaj G, Yoozbashizadeh H, Khodabandeh A, Tamizifar M. Austenite grain growth modelling in weld heat affected zone of Nb/Ti microalloyed linepipe steel. Mater Sci Technol. 2014;30(4):424-33.
10. Khalaj G, Khoeini M, Khakian-Qomi M. ANN-based prediction of ferrite fraction in continuous cooling of microalloyed steels. Neural Comput Appl. 2013;23:769-77.
11. Khalaj G, Pouraliakbar H, Mamaghani KR, Khalaj M. Modeling the correlation between heat treatment, chemical composition and bainite fraction of pipeline steels by means of artificial neural networks. Neural Netw World. 2013;23:351-67.
12. Xavier CR, Delgado HG Jr, Marcelo CJ, Silva FRF, Freitas GCLD, Castro JA. A coupled thermo-mechanical-metallurgical model capturing essential transformations in the welding of high strength low-alloy steels. Soldag Insp. 2021;26(e2617):1-18.
13. Hemmer H, Grong Ø. A process model for the heat-affected zone microstructure evolution in duplex stainless steel weldments: Part I. the model. Metall Mater Trans, A Phys Metall Mater Sci. 1999;30A:2915-29.
14. Ferro P, Bonollo F. A semiempirical model for sigma-phase precipitation in duplex and superduplex stainless Steels. Metall Mater Trans, A Phys Metall Mater Sci. 2012;43:1109-16.
15. Hertzman S, Ferreira PJ, Brolund B. An Experimental and theoretical study of heat-affected zoneaustenite reformation in three duplex stainless steels. Metall Mater Trans, A Phys Metall Mater Sci. 1997;28A:277-85.

16. ASTM: American Society for Testing and Materials. ASTM E-562-19: standard test method for determining volume fraction by systematic manual PointCount. West Conshohocken: ASTM International; 2019.
17. Xavier CR, Delgado HG Jr, Castro JA. Numerical evaluation of the weldability of the low alloy ferritic steels T/P23 and T/P24. Mater Res. 2011;14(1):73-90.
18. Castro JA, Oliveira EM, Almeida DSS, Fonseca GS, Xavier CR. Effects of local heat input conditions on the thermophysical properties of Super Duplex Stainless Steels (SDSS). Mater Res. 2018;1:1-9.
19. Goldak J, Chakravarti A, Bibby M. A new finite element model for welding heat sources. Metall Trans, B, Process Metall. 1984;15(2):299-305.
20. Gunn RN, editor. Duplex stainless steels: microstructure, properties and applications: Cambridge: Abington Publishing; 1997. 216 p.
21. Kim Y-J. Phase transformations in cast duplex stainless steels [thesis]. Ames: Iowa State University; 2004.
22. Kotecki DJ, Siewert TA. Constitution diagram for stainless steel weld metals: a modification of the WRC-1988 diagram. Wel Res Suppl. 1992;5:171s-7s.
23. Muthupandi V, Srinivasan PB, Shankar V, Seshadri SK, Sundaresan S. Effect of nickel and nitrogen addition on the microstructure and mechanical properties of power beam processed duplex stainless steel (UNS 31803) weld metals. Mater Lett. 2005;59(18):2305-9.
24. Atamert S, King JE. Elemental partitioning and microstructural development in duplex stainless steel weld metal. Acta Metall Mater. 1991;39(3):273-85.
25. Ogawa T, Koseki T. Effect of composition profiles on metallurgy and corrosion behavior of duplex stainless steel weld metals. Weld J Res Suppl. 1989;68(5):181s-91s.